The crustal magma reservoir geometry and seismic activity beneath the Wudalianchi volcano in northeast China: Implications for the multilevel magmatic system

Ziqiang Lü[1], Qinghan Kong[1], Jianshe Lei [2], Yinshuang Ai[3]

5   [1]College of Mining, Liaoning Technical University, Fuxin, 123000, China
[2]Key Laboratory of Crustal Dynamics, National Institute of Natural Hazards, Ministry of Emergency Management of China, Beijing, 100036, China
[3]Key Laboratory of Earth and Planetary Physics, Institute of Geology and Geophysics, Chinese Academy of Sciences, Beijing, 100036, China

Correspondence to: Ziqiang Lü(ziqianglyu@sina.com); Jianshe Lei (jshlei_cj@126.com)

Abstract. Understanding the spatial correlation between crustal magma reservoir and seismicity is crucial for investigating the dynamics of volcanic systems. However, due to the relatively low resolution of existing crustal tomography, especially for the middle-lower crustal magma reservoir, it is still difficult to accurately characterize the crustal magma system beneath

15   the Wudalianchi volcano in northeast China. Here, we present a high-resolution 3-D shear-wave velocity crustal model obtained by applying full-wave ambient noise tomography. High-quality empirical Green's functions are extracted from ambient seismic noise at periods of 3-20 s based on 30 latest broadband seismic stations throughout the Wudalianchi volcano. Our new tomographic model reveals a distinct low-velocity body located at depths of ~10-23 km below the Wudalianchi volcano, suggesting the presence of a magma reservoir in the middle-lower crust, which establishes an important link for

20   better understanding of the magma evolution processes. Additionally, the geometry of observed magma reservoir, together with the earthquake distribution, provides new insights into the magmatic activity of the active Wudalianchi volcano. The magma ascent from the potential middle-lower crustal magma reservoir might exert pressure on the overlying brittle crust, resulting in the generation of the earthquakes below the Wudalianchi volcano. The presence of partial melting could make the strength of the surrounding rocks more susceptible to ductile deformation, suggesting that the earthquake nucleation is

25   more difficult within the interior of the crustal magma reservoir beneath the WDLC volcano.

1 Introduction

The magmatic system consists of multi-level complex magma reservoirs and channels for storing and transporting magmatic materials. The middle-lower crustal magma reservoir, as a significant transit station, controls magma storage, accumulation, and differentiation. However, due to the sparse distribution of the seismograph network, the underlying middle-lower crustal

30   magmatic structure of the Wudalianchi (WDLC) volcano remains poorly understood. The WDLC volcano, named for five

connected lava-dammed lakes, is situated on the northern flank of the Songliao Basin in northeast China (Fig. 1). The volcanic field contains 14 cinder cones surrounded by basaltic lava flows (Zhao et al., 2014). The diameters of most cone bases range from 500 to 1200 m and their heights range from 40 to 170 m, and these cones are predominantly arranged along multiple northeast-southwest orientations (Wei et al., 2003). As one of the youngest volcanoes, it has notable volcanic

35 activity. The evolution of the WDLC volcano can be traced back to the early Pleistocene and the latest volcanic activity recorded occurred in ~1721, and the lava flows formed during past eruptions span an area of ~70 square kilometers (Rasskazov et al., 2016). In 1776, the most recent volcanic activity took place in Laoheishan, a sub-volcano within the WDLC volcanic area (Chen et al., 2021).
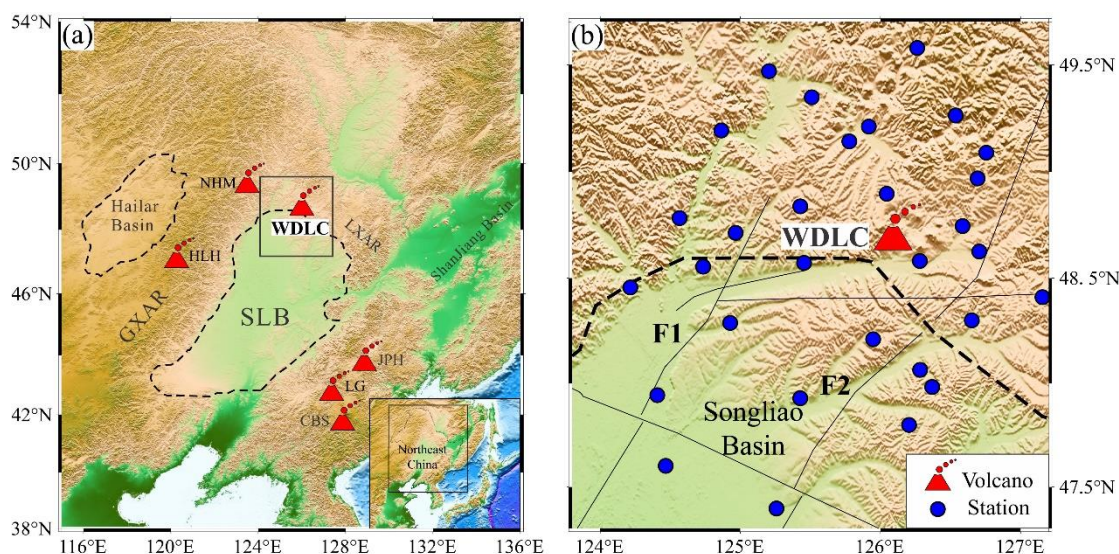
40 **Figure 1: Map view of the surface topography and major tectonic settings of the Wudalianchi (WDLC) volcanic field. The blue circles denote seismic stations used in this study. The dash line and thin black lines mark the outlines of the basins and major faults, respectively. CBS, Changbaishan; HLH, Halaha; LG, Longgang; JPH, Jingpohu; NMH, Nuominhe; SLB, Songliao Basin; GXAR, Great Xing'an range; LXAR, Lesser Xing'an range; F1, Nenjiang fault; F2, Hailun-Renmin fault.**

The distribution of earthquakes under the volcano can provide insights into the development of magmatic activity. An

45 earthquake swarm was detected between 2015 and 2023 in the WDLC volcanic region recorded by the earthquake catalog from the China Earthquake Administration (Fig. 2 and S1). This swarm includes 243 earthquakes and the largest earthquake was magnitude 2.9. The local earthquake locations show that the seismic activities are mainly distributed in the depth range of ~5-15 km beneath the WDLC volcano.
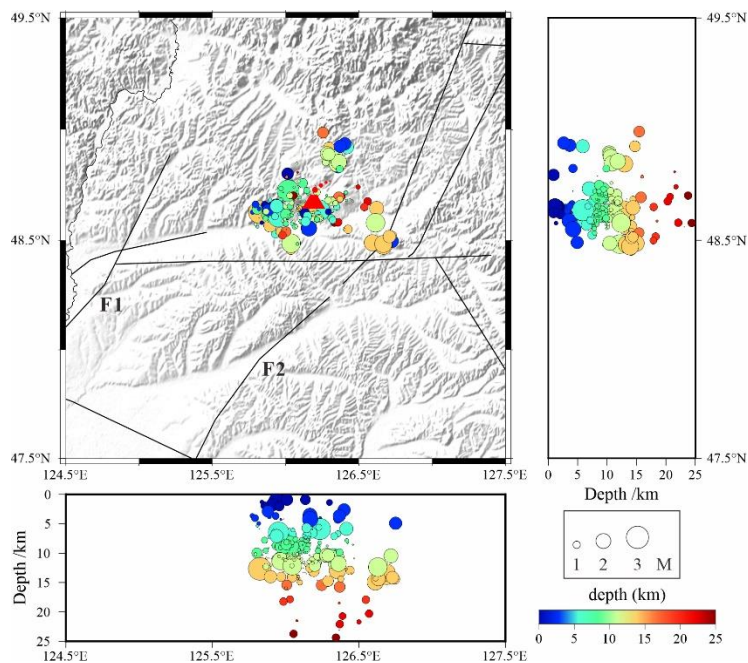
Figure 2: The spatial distribution of the earthquakes in the Wudalianchi volcanic field. The circles denote the earthquakes with different depths and magnitudes. The scales are shown at the right corner.

The intraplate volcanism in northeast China remains a topic of ongoing research and debate, and several different mechanisms have been proposed to explain the formation of intraplate volcanism. Previous body-wave tomographic results have identified significant low-velocity anomalies reaching as low as -3% with a diameter of about 200 km, extending consistently to a depth of 400 km (Lei and Zhao 2005), indicating that the WDLC volcano results from the presence of hot and wet upwelling flows within the big mantle wedge above the subducting Pacific slab located in the mantle transition zone beneath East Asia (Zhao et al. 2007; Zhang and Wu, 2019). Additionally, a continuous slow velocity anomaly down to the mantle transition zone was observed in northeast China, interpreted as the subduction-related mantle upwelling escaped through a slab "gap" in the transition zone (Tang et al., 2014). Ambient noise tomography and two-plane surface wave tomography revealed a downwelling high-velocity anomaly beneath the Songliao Basin, which has the potential to trigger localized convection in the asthenosphere, leading to the formation of local volcanoes (Guo et al., 2006). Numerical simulation results indicate that the Cenozoic volcanic activity in northeast China may be attributed to the interaction between the subducting Pacific plate and the hydrated mantle transition zone (Yang and Faccenda, 2020). However, these hypotheses for the large-scale volcanism are not adequate to fully explain the WDLC volcanism as well as its spatial pattern of seismic activity.

The lithospheric mantle and shallow upper crustal structures have been imaged by previous studies (Li et al. 2016; Liu et al., 2017; Gao et al., 2020; Chen et al., 2021; Fan et al., 2021). The regional-scale lithospheric tomographic results revealed a high-velocity anomaly beneath the WDLC lithospheric mantle, which is likely caused by the interaction between low-degree

melts from the asthenosphere and the underlying subcontinental lithospheric mantle (Fan et al., 2021). In contrast, a
70   prominent low- velocity anomaly is observed extending from the Moho to a depth of 100 km beneath the WDLC volcano,
interpreted as local asthenospheric upwelling (Chen et al., 2021). In general, the underlying lithospheric structures of the
WDLC volcano are still the subject of ongoing debate. Additionally, for the shallow crustal structure, a prominent low-
velocity anomaly is imaged in the upper crust based on a small-scale dense seismic array with ambient noise tomography (Li
et al. 2016), and the low-resistance structures in the upper crust are observed beneath the WDLC volcano by the
75   magnetotelluric imaging based on a dense magnetotelluric network with average site spacing of ~1 km (Gao et al., 2020).
However, small-scale tomographic results are only focused on the upper crustal structures of the volcano. In order to couple
the deep mantle with the shallow upper crustal magmatic systems, a strong understanding of the middle-lower crustal
magmatic structure and its corresponding seismicity is necessary.

Benefiting from the WAVESArray seismic stations deployed in northeast China, more detailed features have been imaged
80   by ray-based ambient noise tomography (Song et al., 2025), and full-wave ambient noise tomography (Lü et al., 2024a; Lü et
al., 2024b). However, the ray-based seismic tomography may affect the resolution of seismic anomalies due to the wavefront
healing effect (Nolet & Dahlen, 2000), especially in resolving small-scale low-V anomaly patterns and amplitudes (Song et
al., 2025). Moreover, the previous full-wave ambient noise tomographic results depicted large-scale seismic features with a
relatively low resolution of ~40 km (Lü et al., 2024a; Lü et al., 2024b), and lacked an analysis of correlation with seismic
85   activity. In this study, we select the denser temporary stations around the WDLC volcanic field and construct a higher
resolution (~27 km) crustal shear-velocity model, which focuses on the geometry of the crustal magma reservoir and spatial
correlation with the seismic activity. Our new finer-scale crustal seismic model can provide more valuable insight into the
magma evolution processes and seismic activity in the WDLC volcanic field.

2 Data and Methods

90   We deployed 30 temporary stations that operated from January 2018 to April 2019, spreading throughout the WDLC
volcano (Fig. 1b). The temporary stations were equipped with three-component seismometers that are capable of measuring
seismic signals over a broad range of frequencies from 50 Hz to 120 seconds, and these instruments record the data with a
high sampling rate of 40 Hz. Due to the dense network of stations (average interstation spacing is ~30 km and the closest
spacing is ~10 km), we can construct a detailed high-resolution shear-wave velocity model beneath the WDLC volcanic
95   field, specifically focusing on understanding the structure and dynamics of the volcanic system and assessing potential
hazards.
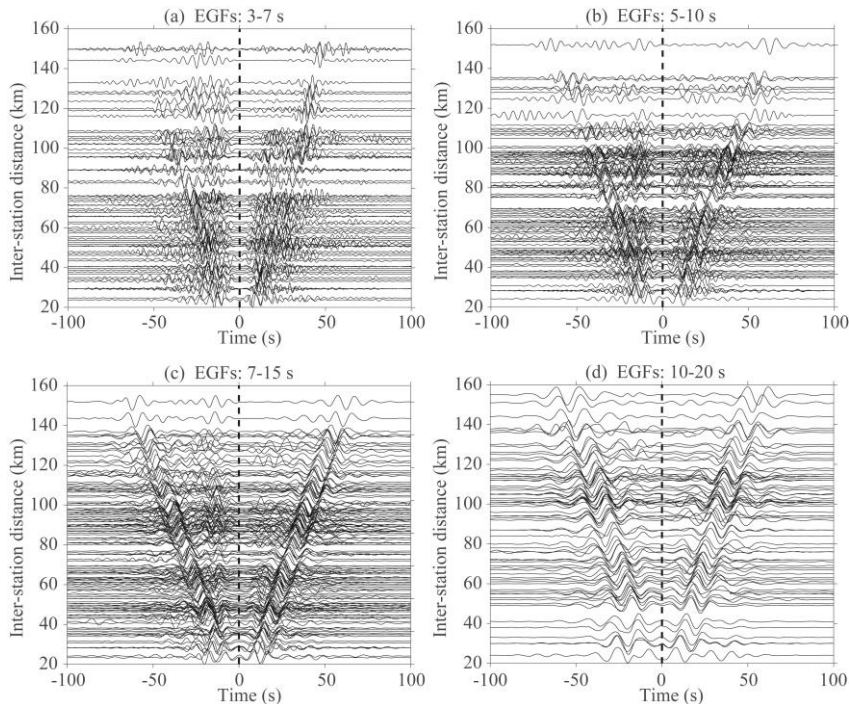
Figure 3: Examples of empirical Green's functions derived from ambient noise data, filtered at (a) 3–7 s, (b) 7–15 s, (c) 7-15 s, and (d) 10-20 s periods, respectively.

100   The cross-correlation of vertical waveforms is used for extraction of the empirical Green's functions (EGFs) between each station pair. After the removal of the instrument responses, the waveforms are downsampled to 5 Hz, and a frequency-time-normalization technique is applied to expand their frequency range (Shen et al., 2012). Specifically, the seismograms are filtered by using a series of narrow-frequency band-pass filters ranging from 0.0125 Hz to 2 Hz. Subsequently, each filtered seismogram is normalized by its envelope and then summed to obtain the final frequency-time normalized seismograms.

105   This technique has been proven to enhance the signal-to-noise ratio of the resultant EGFs, enabling the acquisition of longer-period signals (Lü et al., 2019; Lü et al., 2021). The daily cross-correlations are then stacked to obtain EGFs for each set of stations. The resulting high-quality Rayleigh wave EGFs can be retrieved at different period bands in both positive and negative time lags (Fig. 3). To measure the phase delays of Rayleigh wave EGFs, we cross-correlate the observed EGFs with synthetic waveforms for different periods. We analyze four periods ranging from 10–20 s, 7–15 s, 5–10 s, and 3–7 s (Figs. 4

110   and S2). In contrast to the longer period data (10–20 s, 7–15 s), the shorter period data (5–10 s, 3–7 s) are relatively scattered due to the shallow structure is not well defined. For each period, we only consider EGFs with a signal-to-noise ratio ≥4 and a correlation coefficient of at least 0.7 between the synthetic and observed waveforms. These criteria ensured that the phase delay measurement was based on high-quality data with a strong correlation between the observed EGFs and synthetic signals.
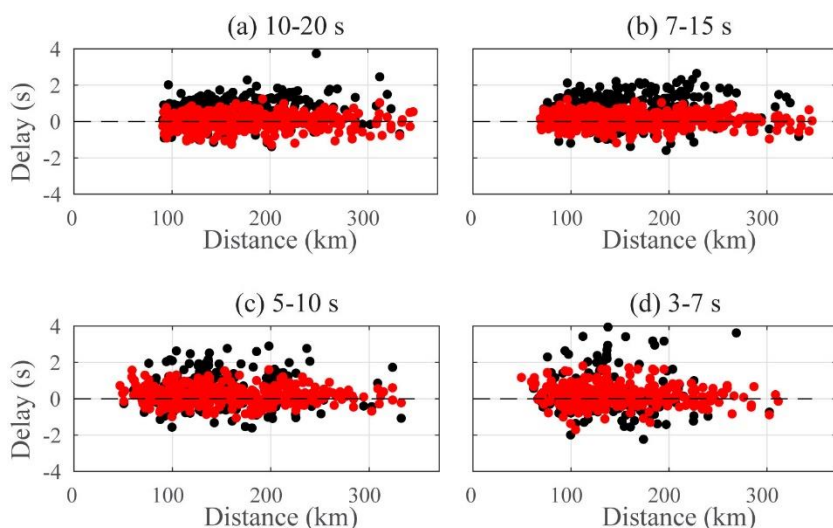
Figure 4: Distribution of phase delays between the observed empirical Green's functions and the synthetics computed using the initial velocity model (black dots) and the final velocity model (red dots). Phase delays are measured at periods of (a) 10-20 s, (b) 7-15 s, (c) 5-10 s, and (d) 3-7 s, respectively.

Waveform propagation in the 3-D heterogeneous Earth's structure is simulated using the non-staggered grid finite-difference method, as described by Zhang et al. (2012). The initial 3-D model is based on a $0.5° \times 0.5°$ shear-wave velocity model underneath mainland China based on surface wave dispersion (Shen et al., 2016). This model has limited resolution to capture detailed variations within the crust due to the limitation of station coverage and the assumption of a one-dimensional layered medium during its construction. We define the initial model grid spanning the region from $47°$ to $50°$ latitude and $123°$ to $128°$ longitude, extending from the Earth's surface down to 199 km depth with a vertical interval of 0.5 km. To enhance the efficiency of the finite-difference algorithm, a non-uniform grid spacing is utilized for discretization. The lateral grid spacing is set at $0.025° \times 0.025°$ in the longitudinal and latitudinal directions, while the vertical grid size varies continuously. The vertical grid interval near the surface is ~0.9 km and increases to ~2.7 km at 25 km depth. The compressional wave velocity and density in the initial model are derived from empirical relationships (Christensen & Mooney, 1995). Synthetic waveforms are calculated using a half width of 4.5 s Gaussian pulse as the source-time function at each station. Updated synthetic waveforms are computed for the iteratively refined 3-D velocity model in each iteration. To cover the longest inter-station distance in the study, a total of 2000 steps are run with a time step of 0.15 seconds to model wave propagation over 300 seconds.

The 3-D finite-frequency sensitivities of the Rayleigh wave are computed for each period band using the scattering-integral method (Zhao et al., 2005). This approach can be utilized to establish an accurate high-resolution 3-D velocity model in comparison with the ray theory. Both P and S waves contribute to the Rayleigh wave propagation, especially in the shallower layers (Gao & Shen, 2014; Lü et al., 2019). Our method involves analyzing sensitivity kernels for both P and S

wave velocities in the joint inversion, providing enhanced constraints on shallow crustal properties and yielding more precise and reliable solutions for deeper structures (Lü & Lei, 2022). Density was not explicitly included in the inversion process. However, density is updated through an empirical relationship between the compressional wave velocity and density 140 (Christensen & Mooney, 1995). During each iteration, new sensitivity kernels were calculated by simulating wave propagation with the updated velocity model. Following the construction of sensitivity kernels, the joint inversion is solved using the LSQR algorithm with a series of damping and smoothing constraints (Paige & Saunders, 1982). We select the optimal smoothing and damping parameters based on the tradeoff between the model norm and data misfit (Fig. S3). The velocity perturbations are then updated and added to the 3-D reference model after each iteration.

145
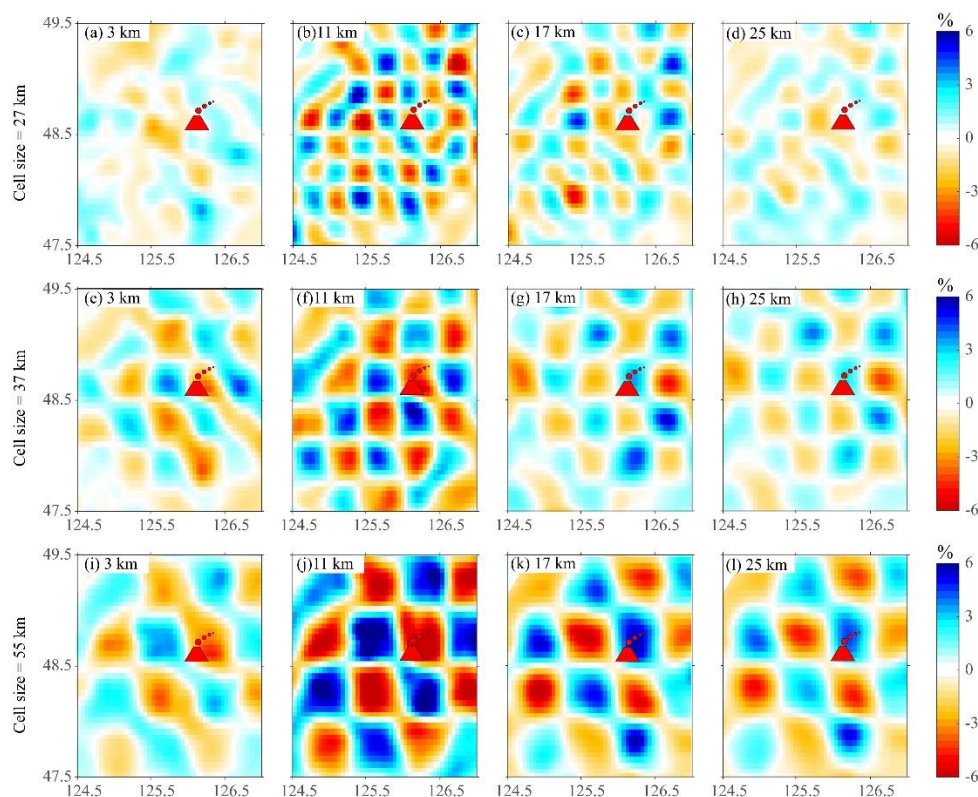
Figure 5: Checkerboard resolution tests at multiple depths for the shear wave velocity models. The velocity perturbation varies within a range of ±6%.

3 Results

150 By incorporating the latest temporary broadband seismic array, the high-resolution seismic features at finer scales have been significantly enhanced. To qualitatively assess the spatial resolution scale, a series of checkerboard tests are conducted at

different depths (Fig. 5). The checkerboard input models are designed with ±6% alternating velocity perturbations at varying depths. The synthetic phase delays are determined by utilizing the sensitivity kernels that are calculated from the last iteration. The checkerboard resolution tests revealed that the input model exhibits excellent recoverability at depths ranging

155 from 11 to 17 km with different cell sizes (Fig. 5). At 3 km depth, the input velocity perturbations can be well resolved with a cell size larger than 37 km. The amplitude of the checkerboard pattern appears to be underestimated at shallow (3 km) and lower crustal depths (25 km) due to the reduction of data for shorter (3-7 s) and longer (10-20 s) periods. Overall, the checkerboard tests demonstrate that the small-scale crustal features with a horizontal scale larger than 27 km can be effectively resolved in the upper-middle crust where most earthquakes are prone to generate. In addition, to further validate

160 the credibility of a significant low-velocity feature, we carry out a specific model recovery test in terms of the anomaly pattern (Fig. S4). The pattern and magnitude of the anomaly can be well recovered with a minor amount of unavoidable smearing at corresponding depths. Our resolution tests indicate that the observed key structural features beneath the WDLC volcanic field are reliable based on the current dense broadband seismic array data coverage.
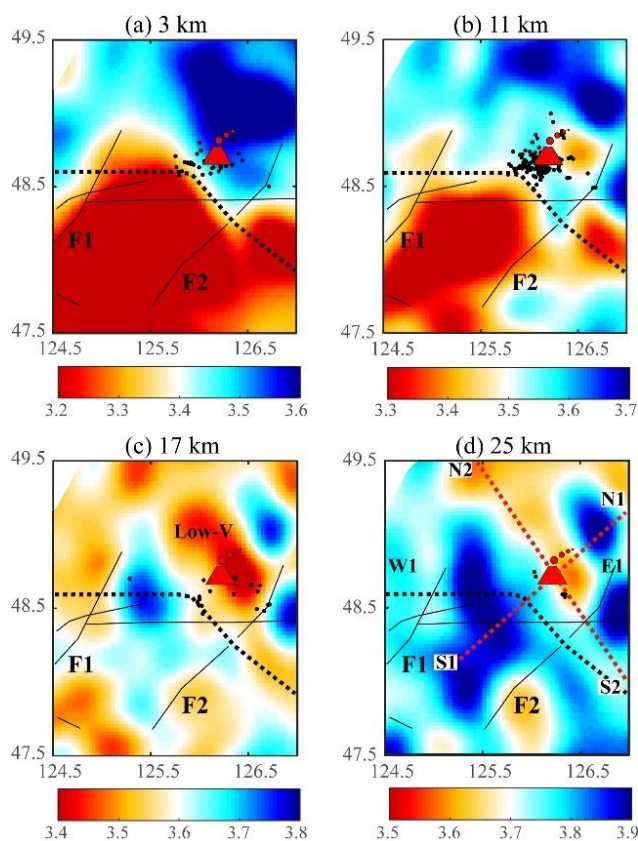
165 **Figure 6: Shear-wave velocity structures at multiple depths. The red dash lines in (d) mark the profile locations in Figure 7. The black dots represent the earthquakes beneath the WDLC volcano. Other labels are the same as those in Figure 1.**

Our new shear-wave velocity model reveals remarkable details in seismic velocity features at various depths (Fig. 6). The obvious low-velocity anomalies are observed beneath the Songliao Basin, whereas high-velocity anomalies are visible under

170 the mountain ranges at a depth of 3 km. The low-velocity anomalies beneath the Songliao Basin are gradually concentrated between the Nenjiang fault (F1) and Hailun-Renmin fault (F2) at 11 km depth. At the middle-lower crust, a distinct low-velocity anomaly exists beneath the WDLC volcano, extending from 17 km down to about 25 km depth, contrasting with strong high-velocity anomalies imaged between the F1 and F2 faults (Fig. 6). The strong lateral variations of the shear-wave velocity contrast underlying the WDLC volcano within the crust are prominently imaged in the vertical cross-sections (Fig.

175 7). Beneath the WDLC volcano, we observe significant low-velocity features at depths of ~10-23 km. The velocity below the Songliao Basin is prominent lower than the regional average within the study area. The earthquakes are mainly located in the low-velocity anomalies or the transition zones from low-velocity to high-velocity anomalies in the upper-middle crust.
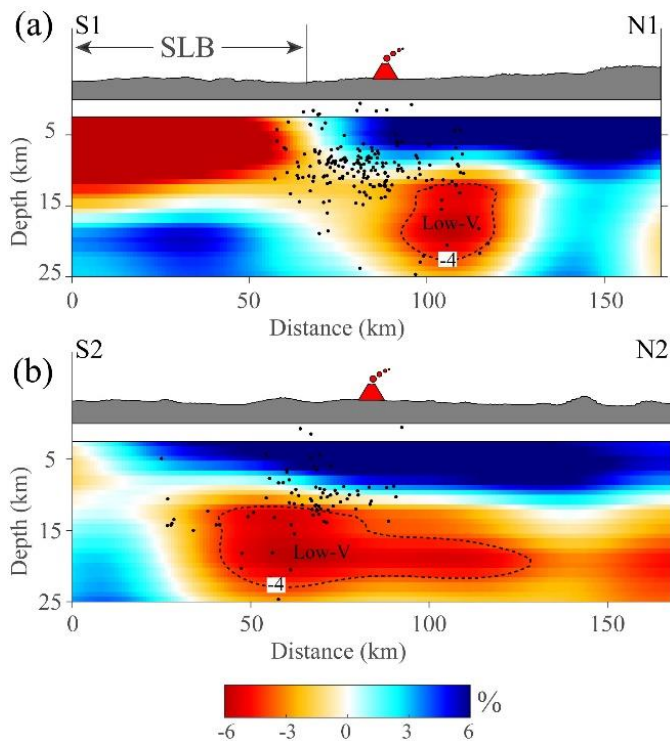
Figure 7: Cross-section view of the shear-wave velocity model and the distribution of the earthquakes. See Figure 6(d)
180 **for the profile locations. Topographic elevation is plotted atop each cross-section. The black dots represent the earthquakes in the study region. The dashed line represent the -4% velocity reduction boundary in each cross-section.**

4 Discussion

4.1 Comparison with recent shear-wave velocity models

Our new shear-wave velocity model reveals seismic features showing tight correlations with the major elements of the
185 WDLC volcanic field at various depths, in comparison with recent shear-wave velocity models from traditional ambient
noise tomography (Figs. 8 and S5), such as Shen et al. (2016), Fan et al. (2021), Chen et al. (2021), and Song et al. (2025).
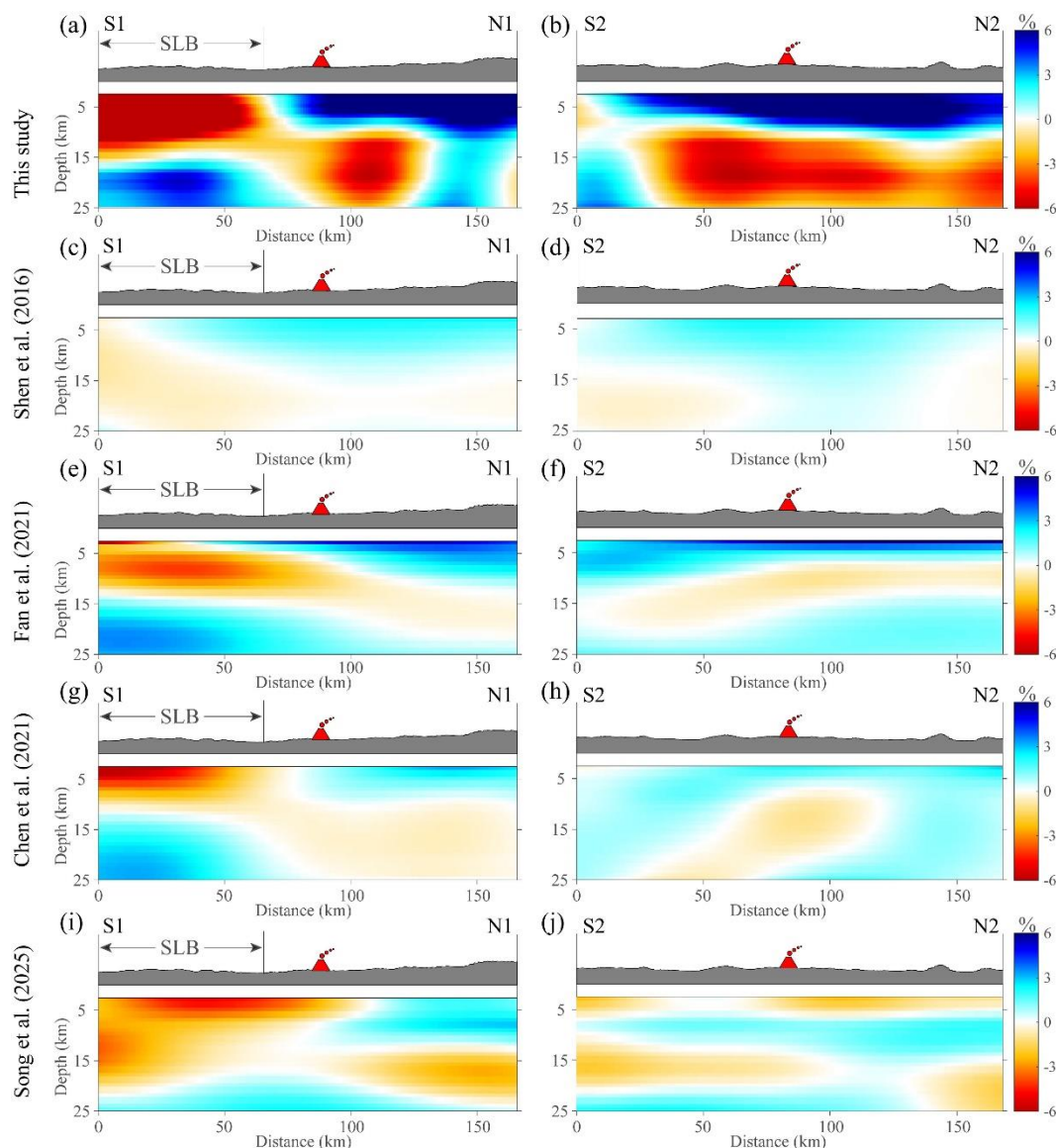
Figure 8:Comparison of cross-sections between our shear-wave velocity model and recent shear-wave velocity models. The symbols are the same as in Figure 7.

190   The traditional ambient noise tomography is based on the ray-based inversion method and assumes that the Rayleigh wave phase velocity is mainly sensitive to shear wave velocity. However, due to wavefront healing (Nolet & Dahlen, 2000), the recovered shear-wave anomalies could be decreased by a factor of two or more (Maguire et al., 2022). The full-wave methods simulate the synthetic waveforms accounting for the physics of seismic wave propagation in the 3-D Earth model, calculate numerical sensitivity kernels, and iteratively invert the shear-wave velocity structure. Theoretically, the full-wave

195   method is more accurate to obtain a high-resolution model (Nolet & Dahlen, 2000; Maguire et al., 2022; Gao & Shen, 2014; Lü et al., 2019). For example, at 3 km depth, compared with recent shear-wave velocity models that demonstrate pervasive low-velocity anomalies surrounding the Songliao Basin, our model reveals obvious low-velocity anomalies corresponding to the outline of the Songliao Basin (Fig. S5). At the depths of 17-25 km, our model demonstrates distinct low-velocity anomalies beneath the WDLC volcano compared with the shear-wave velocity from the recent models. Moreover, our model

200   also reveals some new seismic features. The F1 and F2 faults are significant velocity contrast boundaries at a depth of 11-25 km. In the vertical cross-sections (Fig. 8), our model reveals a circular low-velocity body in the middle-lower crust, which clearly reflects the shape of the middle-lower crustal magma reservoir. It is noted that this feature was not clearly identified by the recent models. Those observations reveal remarkable details in seismic velocity features and provide a tighter spatial linkage with the underlying volcanic system.

205   **4.2 Correlation with seismicity**

The spatial distribution of earthquakes provides insights into the development of magmatic activity. Earthquake activity beneath a volcano typically increases prior to an eruption due to the movement of magma and gases, which exert pressure on the surrounding rocks, leading to the fracturing of rocks or the vibration of existing cracks (Roman & Cashman, 2018). The earthquake activity beneath the WDLC volcano appears to be strongly influenced by the observed features in the shear-wave

210   velocity model (Fig. 7). The earthquakes are located in relatively large velocity gradients above the middle-lower crustal magma reservoir beneath the WDLC volcano. This spatial association is interpreted as stress concentration at structural discontinuities induced by magmatic processes such as magma ascent. The magma ascent exerts pressure on the overlying brittle crust, resulting in the generation of the earthquakes (Kiser et al., 2016; Korger & Schlindwein, 2014). Notably, a few earthquakes occurred in the center of the low-velocity body of the middle-lower crustal magma reservoir. The likely average

215   melt fraction is ~3.5 % in the middle-lower crustal magma reservoir deriving from the relationship between shear-wave velocity and melt fraction (Lü et al., 2024b). The presence of partial melt within the magma reservoir could make the strength of the surrounding rocks more susceptible to ductile deformation, implying that the earthquake nucleation is more difficult within the middle-lower crustal magma reservoir beneath the WDLC volcano. Therefore, combining the seismicity and our observed low-velocity structures, we suggest that the magma upward migration from the middle-lower crustal

220   magma reservoir would drive rock fracturing above the magma reservoir, which might be responsible for the earthquakes beneath the WDLC volcano.

4.3 Implication for multi-level magmatic system

Here we propose a schematic model to illustrate the key seismic features observed beneath the WDLC volcano as well as possible interpretations based on our and recent shear-wave models (Fig. 9). However, we cannot rule out other possible
225 causes for the deep magmatic system. The geometry of the observed middle-lower crustal magma reservoir beneath the WDLC volcano plays a key role in understanding magma accumulation and feeding systems, which may establish an important link for better defining the volcanic dynamics from deep mantle to shallow crust. Deep mantle-scale tomographic studies revealed a low-velocity anomaly down to about 410 km depth beneath the WDLC volcano (Lei & Zhao, 2005; Zhao et al., 2007; Zhang & Wu, 2019). According to the lithospheric-scale tomography study, a prominent channel-like low-
230 velocity body was identified extending from the Moho to a depth of 100 km beneath the WDLC volcano (Chen et al., 2021). Comparatively, Li et al. (2016) discovered a low-velocity zone at upper crust depth (~7-13 km) beneath a sub-volcano in the WDLC volcanic region based on a short-period dense seismic array with ambient noise tomography. By combining our new model with previous tomographic images, we present a possible comprehensive understanding of the volcanic genesis of the WDLC volcano. The origin of the WDLC volcano is associated with the upwelling of asthenospheric materials within the
235 big mantle wedge (Lei & Zhao, 2005). Geochemical research on rocks in the WDLC volcanic field demonstrates that the magma originates from the mantle transition zone, directly linked to the stagnation of the deeply subducted western Pacific slab (Wang et al., 2017). Subsequently, the rising asthenospheric material accumulates at the base of the lithosphere as a mantle magma reservoir, feeding the WDLC volcano and neighboring volcanoes (Chen et al., 2021). This inference is also supported by the Pn tomographic result that observed a low-velocity zone in the uppermost mantle beneath the WDLC
240 volcanic field in northeast China (Du et al., 2022). After a long period of accumulation, the mantle magma penetrated the uppermost mantle into the middle-lower crustal magma reservoir, corresponding with our observed low-velocity anomalies in the crust beneath the WDLC volcano. Given that the last eruption of a sub-volcano in the WDLC volcanic region occurred approximately 300 years ago, combined with the constraints from the deep mantle, lithosphere, and upper crustal structures, our observed middle-lower crustal magma reservoir could potentially act as a significant reservoir for recharging the shallow
245 magma reservoir in the upper crust. Furthermore, a well in the region exhibits an exceptionally high CO_2 concentration, further indicating the activity of the WDLC volcano (Lü, 1994). In general, the active intraplate WDLC volcano demonstrates a vertical multi-level magma system from the mantle source to the upper crust (Fig. 9). The upwelling asthenospheric material driven by the deep subduction and stagnation of Pacific slab ponds at the lithospheric base, then migrates to the middle-lower crustal magma reservoir that supplies the upper crustal magma reservoir. The observed middle-
250 lower crustal magma reservoir establishes a robust connection between the accumulation of mafic magmas and the generation of melts to supply the upper crustal magma reservoir as imaged by Li et al. (2016).
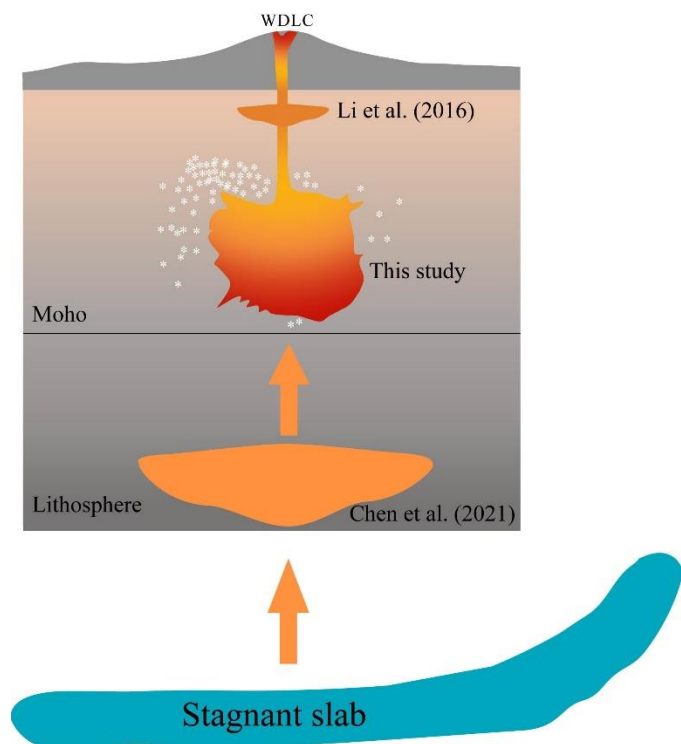
Figure 9: A schematic diagram illustrating the vertical multi-level magma system and seismicity beneath the WDLC volcano. Illustrations here are not to scale. The magma ascent from our observed middle-lower crustal magma reservoir may exert pressure on the overlying brittle crust, resulting in the generation of the earthquakes below the WDLC volcano. The white stars represent the earthquakes. The lithospheric magma reservoir was imaged by Chen et al. (2021) and the upper crustal magma reservoir was imaged by Li et al. (2016).

5 Conclusions

The spatial correlation between the middle-lower crustal magma reservoir and the seismicity of the WDLC volcano plays a crucial role in understanding the magmatic system and potential hazards. In this study, we construct a high-resolution crustal shear-wave velocity model beneath the WDLC volcanic field using the full-wave ambient noise tomographic method based on our latest temporary stations. Our tomographic model reveals a distinct low-velocity body existing at depths of ~10-23 km beneath the WDLC volcano, indicating the middle-lower crustal magma reservoir with an average estimated melt fraction of ~3.5%. The earthquakes beneath the WDLC volcano are located above the crustal magma reservoir revealed by this study, suggesting the active volcanic seismicity could be related to the magma upward migration deriving from the crustal magma reservoir. By combining the existing velocity models in different scales, the WDLC intraplate volcanism might be related to the multi-level magmatic system from deep mantle to shallow crust. These new findings provide valuable

perspectives on the WDLC volcanic monitoring and hazard assessment for future eruption.

270 **Data Availability**

The seismic waveform data used in the study are archived in a repository (https://doi.org/10.5281/zenodo.11609148).

Author contributions

ZL and JL were responsible for the conception of this study. QK analysed the data. JL and AY were responsible for designing the network. ZL prepared the paper, and all authors critically reviewed it. All authors also contributed to reviewing

275 and editing the paper.

Competing interests

The authors declare that they have no conflict of interest.

Disclaimer

Publisher's note: Copernicus Publications remains neutral with regard to jurisdictional claims made in the text, published

280 maps, institutional affiliations, or any other geographical representation in this paper. While Copernicus Publications makes every effort to include appropriate place names, the final responsibility lies with the authors.

Acknowledgments

This research was supported by the National Natural Science Foundation of China (U1939206, 42274129, 41530212, and 41674091).

285 **References**

Chen, Y., Ai, Y., Jiang, M., Yang, Y., and Lei, J.: New insights into potassic intraplate volcanism in Northeast China from joint tomography of ambient noise and teleseismic surface waves, J. Geophys. Res.-Sol. Ea., 126, e2021JB021856, 2021.

Christensen, N. I. and Mooney, W. D.: Seismic velocity structure and composition of the continental crust: A global view, J. Geophys. Res., 100(B6), 9761-9788, 1995.

290 Du, M., Lei, J., Zhao, D., and Lu, H.: Pn anisotropic tomography of Northeast Asia: New insight into subduction dynamics and volcanism, J. Geophys. Res.-Sol. Ea., 127, e2021JB023080, 2022.

Fan, X., Chen, Q., Ai, Y., Chen, L., Jiang, M., Wu, Q., and Guo, Z.: Quaternary sodic and potassic intraplate volcanism in northeast China controlled by the underlying heterogeneous lithospheric structures, Geology, 49, 1260-1264, 2021.

Gao, H. and Shen, Y.: Upper mantle structure of the Cascades from full-wave ambient noise tomography: Evidence for 3D

295 mantle upwelling in the back-arc, Earth Planet. Sc. Lett., 390, 222-233, 2014.

Gao, J., Zhang, H., Zhang, S., Xin, H., Li, Z., Tian, W., Bao, F., Cheng, Z., Jia, X., and Fu, L.: Magma recharging beneath the Weishan volcano of the intraplate Wudalianchi volcanic field, northeast China, implied from 3-D magnetotelluric imaging, Geology, 48, 913-918, 2020.

Guo, Z., Chen, Y., Ning, J., Yang, Y., Afonso, J.C., and Tang, Y.: Seismic evidence of ongoing sublithosphere upper mantle convection for intraplate volcanism in Northeast China, Earth Planet. Sc. Lett., 433, 31-43, 2016.

Kiser, E., Palomeras, I., Levander, A., Zelt, C., Harder, S., Schmandt, B., Hansen, S., Creager, K., and Ulberg C.: Magma reservoirs from the upper crust to the moho inferred from high-resolution V_P and V_S models beneath Mount St. Helens, Washington State, USA, Geology, 44(6), 411-414, 2016.

Korger, E. and Schlindwein, V.: Seismicity and structure of the 85°E volcanic complex at the ultraslow spreading Gakkel Ridge from local earthquake tomography, Geophys. J. Int., 196(1), 539–551, 2014.

Lei, J. and Zhao, D.: P-wave tomography and origin of the Changbai intraplate volcano in Northeast Asia, Tectonophysics, 397, 281-295, 2005.

Li, Z., Ni, S., Zhang, B., Bao, F., Zhang, S., Deng, Y., and Yuen, D.A.: Shallow magma chamber under the Wudalianchi Volcanic Field unveiled by seismic imaging with dense array, Geophys. Res. Lett., 43, 4954-4961, 2016.

Liu, Y., Niu, F., Chen, M., and Yang, W.: 3-D crustal and uppermost mantle structure beneath NE China revealed by ambient noise adjoint tomography, Earth Planet. Sc. Lett., 461, 20-29, 2017.

Lü, Z., Gao, H., Lei, J., Yang, X., Rathnayaka, S., and Li, C.: Crustal and upper mantle structure of the Tien Shan orogenic belt from full-wave ambient noise tomography, J. Geophys. Res.-Sol. Ea., 124, 3987-4000, 2019.

Lü, Z. and Lei, J.: Seismic evidence for crustal modification across the Tanlu fault zone in eastern China, Geophys. Res. Lett., 49, e2022GL099761, 2022.

Lü, Z., Lei, J., Zhao, L., Fu, X., Chen, J., Li, G., and Kong, Q.: Crustal deformation of intermontane basins beneath Central Tien Shan revealed by full-wave ambient noise tomography, Tectonophysics, 821, 229143, 2021.

Lü, Z., Lei, J., Zhao, D., Xu, Y., Liu, L., Sun, C., Ai, Y., and Taymaz, T.: The magmatic plumbing beneath the Wudalianchi volcanic region, northeast China, is recharged by magma reservoirs under Keluo volcano. Commun. Earth Environ., 5, 575, 2024a.

Lü, Z., Lei, J., and Yang, X.: Seismic structure of the Wudalianchi volcanic field in Northeast China: insights into magma reservoir and crustal magmatic plumbing systems. Bulletin of Volcanology, 86:92, 2024b.

Lü, Z.: Volcanic structure of the present-day volcanic group Wudalianchi and its forming mechanism, Volcanology and Mineral Resources, 15, 6-21,1994.

Maguire, R., Schmandt, B., Chen, M., Jiang, C., Li, J., and Wilgus, J.: Resolving continental magma reservoirs with 3D surface wave tomography, Geochem. Geophys. Geosys., 23, e2022GC010446, 2022.

Nolet, G. and Dahlen, F.: Wave front healing and the evolution of seismic delay times, J. Geophys. Res., 105, 19043-19054, 2000.

Paige, C. and Saunders, M.: LSQR: An algorithm for sparse linear equations and sparse least squares, ACM Trans. Math. Software, 8(1), 43–71, 1982.

Rasskazov, S.V., Chuvashova, I.S., Sun, Y.-M., Yang, C., Xie, Z., Yasnygina, T.A., Saranina, E.V., and Fang, Z.: Sources of Quaternary potassic volcanic rocks from Wudalianchi, China: Control by transtension at the lithosphere-asthenosphere boundary layer. Geodynamics & Tectonophysics, 7, 555-592, 2016.

Roman, D. C. and Cashman, K. V.: Top-down precursory volcanic seismicity: Implications for 'Stealth' magma ascent and long-term eruption forecasting. Frontiers in Earth Science, 6, 124, 2018.

Shen, W., Ritzwoller, M., Kang, D., Kim, Y., Lin, F., Ning, J., Wang, W., Zheng, Y., and Zhou, L.: A seismic reference model for the crust and uppermost mantle beneath China from surface wave dispersion. Geophys. J. Int., 206(2), 954-979, 2016.

Shen, Y., Ren, Y., Gao, H., and Savage, B.: An improved method to extract very-broadband empirical Green's functions from ambient seismic noise, B. Seismol. Soc. Am., 102(4), 1872-1877, 2012.

Song, X., Lei, J., Zhao, D., and Ai, Y.: Crust and uppermost mantle S-wave velocity structure of the Wudalianchi volcanic belt from direct surface-wave tomography. Journal of Asian Earth Sciences, 278, 106426, 2025.

Tang, Y., Obayashi, M., Niu, F., Grand, S. P., Chen, Y. J., Kawakatsu, H., Tanaka, S., Ning, J., and Ni, J.:Changbaishan volcanism in northeast China linked to subduction-induced mantle upwelling, Nat. Geosci., 7(6), 470–475, 2014.

Wang, X., Chen, L., Hofmann, A., Mao, F., Liu, J., Zhong, Y., Xie, L., and Yang, Y.: Mantle transition zone–derived EM1 component beneath NE China: Geochemical evidence from Cenozoic potassic basalts, Earth Planet. Sc. Lett., 465, 16-28, 2017.

Wei, H., Sparks, R., Liu, R., Fan, Q., Hong, H., Zhang, H., Chen, H., Jiang, C., Dong, J., Zheng, Y., and Pan, Y.:Three active volcanoes in China and their hazards, Journal of Asian Earth Sciences, 21,515-526, 2003.

Yang, J. and Faccenda, M.: Intraplate volcanism originating from upwelling hydrous mantle transition zone, Nature, 579, 88-91, 2020.

Zhang, F. and Wu, Q.: Velocity structure in upper mantle and its implications for the volcanism nearby the north edge of Songliao Basin, Chin, J. Geophys. 62, 2918–2929, 2019.

Zhang, W., Shen, Y., and Zhao, L.: Three-dimensional anisotropic seismic wave modeling in spherical coordinate by a collocated-grid finite difference method, Geophys. J. Int., 188(3), 1359-1381, 2012.

Zhao, D., Maruyama, S., and Omori, S.: Mantle dynamics of Western Pacific and East Asia: Insight from seismic tomography and mineral physics, Gondwana Research, 11, 120-131, 2007.

Zhao, L., Jordan, T. H., Olsen, K. B., and Chen, P.: Fréchet kernels for imaging regional Earth structure based on three-dimensional reference models, B. Seismol. Soc. Am., 95(6), 2066-2080, 2005.

Zhao, Y., Li, N., Fan, Q., Zou, H., and Xu, Y.: Two episodes of volcanism in the Wudalianchi volcanic belt, NE China: Evidence for tectonic controls on volcanic activities, Journal of Volcanology and Geothermal Research, 285, 170-179, 2014.